Geophysical Research Letters

RESEARCH LETTER
10.1029/2018GL079406

Key Points:
- Upper mantle Rayleigh and *S* wave tomography using the full Transportable Array in Alaska
- Thick high Vs lithosphere is found beneath the western Brooks Range and Arctic coast
- A high Vs potential slab fragment is identified beneath the Wrangell volcanic field

Supporting Information:
- Supporting Information S1

Correspondence to:
C. Jiang,
chengxinjiang@gmail.com

Citation:
Jiang, C., Schmandt, B., Ward, K. M., Lin, F.-C., & Worthington, L. L. (2018). Upper mantle seismic structure of Alaska from Rayleigh and *S* wave tomography. *Geophysical Research Letters*, *45*, 10,350–10,359. https://doi.org/10.1029/2018GL079406

Received 28 JUN 2018
Accepted 21 SEP 2018
Accepted article online 27 SEP 2018
Published online 10 OCT 2018

Upper Mantle Seismic Structure of Alaska From Rayleigh and *S* Wave Tomography

Chengxin Jiang[1], Brandon Schmandt[1], Kevin M. Ward[2,3], Fan-Chi Lin[2], and Lindsay L. Worthington[1]

[1]Department of Earth and Planetary Sciences, The University of New Mexico, Albuquerque, NM, USA, [2]Department of Geology and Geophysics, The University of Utah, Salt Lake City, UT, USA, [3]Now at Department of Geology and Geological Engineering, South Dakota School of Mines and Technology, Rapid City, SD, USA

Abstract Mantle shear velocity (Vs) structure beneath the Transportable Array (TA) in Alaska and northwestern Canada is imaged by joint inversion of Rayleigh wave dispersion and teleseismic *S* wave travel times. The study connects previously unsampled parts of northern and western Alaska with portions of southern Alaska imaged with earlier seismic arrays. The new Vs tomography shows contrasting lithospheric structure in the plate interior with lower Vs shallow upper mantle indicative of thinner thermal lithosphere south of the Brooks Range and along the transform margin. Higher Vs down to ~200 km beneath the Brooks Range and northern coast is consistent with the presence of a cold stable lithospheric root that may help guide intraplate deformation to the south. In the subduction-to-transform transition, a potential slab fragment is imaged beneath the Wrangell volcanic field where modern subduction has slowed due to the thick buoyant crust of the Yakutat terrane.

Plain Language Summary We use a groundbreaking seismic data set from the EarthScope project to investigate the structure of the upper mantle beneath Alaska and northwestern Canada to better understand the effects of ongoing subduction and distinctive blocks within the continental lithosphere. Measurements of seismic body and surface waves are used to construct seismic images from the surface down to 800-km depth. The images reveal cold thick blocks beneath northern Alaska and the Yukon Territory adjacent to warmer thinner blocks beneath younger geologic provinces to the south, suggesting that cold strong lithosphere in the north helps guide the extent of intraplate deformation driven by the southern plate boundary. The model also identifies a potential slab fragment beneath the Wrangell volcanic field, suggesting slab contributions to volcanic activity and a growing slab tear.

1. Introduction

Plate boundary processes have shaped the lithosphere of Alaska from the Mesozoic to the present with multiple episodes of terrane accretion, arc magmatism, and inboard propagation of crustal deformation driven by evolving southern plate boundary dynamics (Jadamec et al., 2013; Mazzotti & Hyndman, 2002; Plafker & Berg, 1994; Trop & Ridgway, 2007). The modern subduction zone extends ~2,500 km along-strike with normal-dip subduction fueling magmatism from the Aleutian arc to the Cook Inlet and an eastward transition to shallow-dip subduction of the Yakutat terrane's thick oceanic crust (Figure 1; Eberhart-Phillips et al., 2006; Hayes et al., 2012; Worthington et al., 2012). Inboard propagation of crustal deformation and the Denali volcanic gap provide surface evidence of ongoing shallow-dip subduction (Haeussler, 2008), which is further documented by earthquake hypocenters and seismic imaging (e.g., Eberhart-Phillips et al., 2006). Increasingly thick Yakutat crust to the east impedes subduction and focuses continental deformation in the corner-shaped transition to a right-lateral transform plate boundary, creating extreme topographic relief and rapid exhumation in the St. Elias Range since ~6 Ma (Elliott et al., 2013; Enkelmann et al., 2015; Marechal et al., 2015; Spotila & Berger, 2010). Stress transfer due to relative motions of the Pacific and North American plates and ongoing accretion of the Yakutat terrane drives broadly distributed seismicity within the plate interior (Figure 2; Leonard et al., 2008). Intraplate deformation constrained by modern geodesy extends inboard to the southern edge of the western Brooks Range and to near the Arctic coast in the eastern Brooks Range and Richardson Mountains (Leonard et al., 2008). Quaternary intraplate magmatism also extends >500 km from the subduction zone margin (Miller et al., 1998). Continuous upper mantle seismic imaging across the region

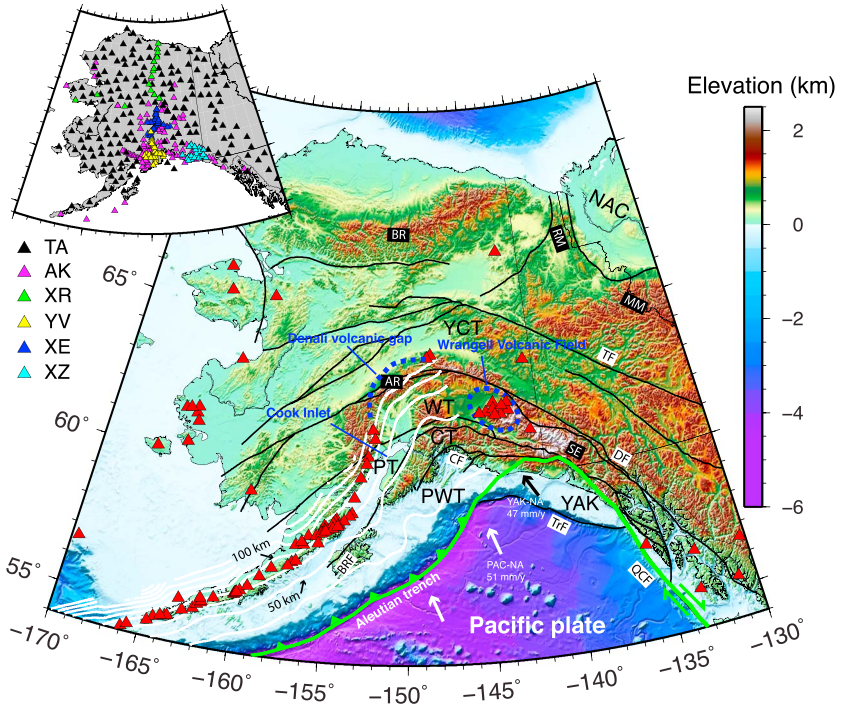

Figure 1. Study area map with the inset showing the seismograph locations (Table S1 in the supporting information). In the main figure, red triangles denote <2 Ma volcanoes. The white lines show the slab 1.0 model (Hayes et al., 2012), and the thick green line marks the Pacific plate boundary. Velocity vector is from DeMets and Dixon (1999) for the Pacific and from Elliott et al. (2010) for the Yakutat. Black thin lines represent major faults separating the NAC = North American Craton, YAK = Yakutat terrane, PWT = Prince William terrane, PT = Peninsular terrane, CT = Chugach terrane, WT = Wrangellia terrane, and YCT = Yukon composite terrane. Major faults include TF = Tintina fault, DF = Denali fault, CF = Contact fault, BRF = Border Ranges fault, TrF = Transition fault and QCF = Queen Charlotte fault. Mountain ranges are labeled as BR = Brooks Range, RM = Richardson Mountain, MM = Mackenzie Mountain, AR = Alaska Range, and SE = St Elias Range.

would enable further investigation of how the current plate boundary system and history of lithospheric assembly control ongoing deformation and magmatism.

In mid-2017, EarthScope's Transportable Array (TA) of broadband seismographs reached its full extent across Alaska and northwest Canada, providing new opportunities for integrated imaging of active subduction and mantle signatures of prior plate boundary evolution (Figure 1). There is a long history of seismic research on Alaskan crust and upper mantle structure including active and passive source studies (e.g., Bauer et al., 2014; Coulson et al., 2018; Eberhart-Phillips et al., 2006; Fuis et al., 2008; Kim et al., 2014; Martin-Short et al., 2016; McNamara & Pasyanos, 2002; Stachnik et al., 2004; Wang & Tape, 2014; You & Zhao, 2012; Zhao et al., 1995), but the vast area and challenges in accessibility limited prior imaging to subset areas and transects. New coverage from the TA provides a coherent large-scale context for synthesis of previously isolated study areas. Outstanding questions include the links between subduction and volcanism in the Wrangell volcanic field (Martin-Short et al., 2016; Page et al., 1989; Preece & Hart, 2004; Richter et al., 1990), the mantle underpinnings of intraplate volcanism in western and central Alaska (Miller et al., 1998), and the degree to which sutured crustal terranes are rooted by distinctive lithospheric structures that may influence ongoing intraplate deformation (e.g., O'Driscoll & Miller, 2015; Saltus & Hudson, 2007).

This study uses the combined sensitivity of Rayleigh and *S* waves to image the shear velocity (Vs) structure of the upper mantle beneath the TA in Alaska and northwestern Canada. Joint inversion of surface and body wave measurements enables deeper imaging than is possible with surface waves alone and mitigates the weaker depth resolution of teleseismic body wave tomography in the uppermost mantle (Golos et al., 2018; Guo et al., 2018; Jiang et al., 2018; Obrebski et al., 2011; West et al., 2004). The resulting images identify a thick lithospheric root beneath the Brooks Range and Arctic coast adjacent to lower Vs in the upper mantle beneath younger accreted terranes to the south and identify a potential slab fragment beneath the Wrangell volcanic field.

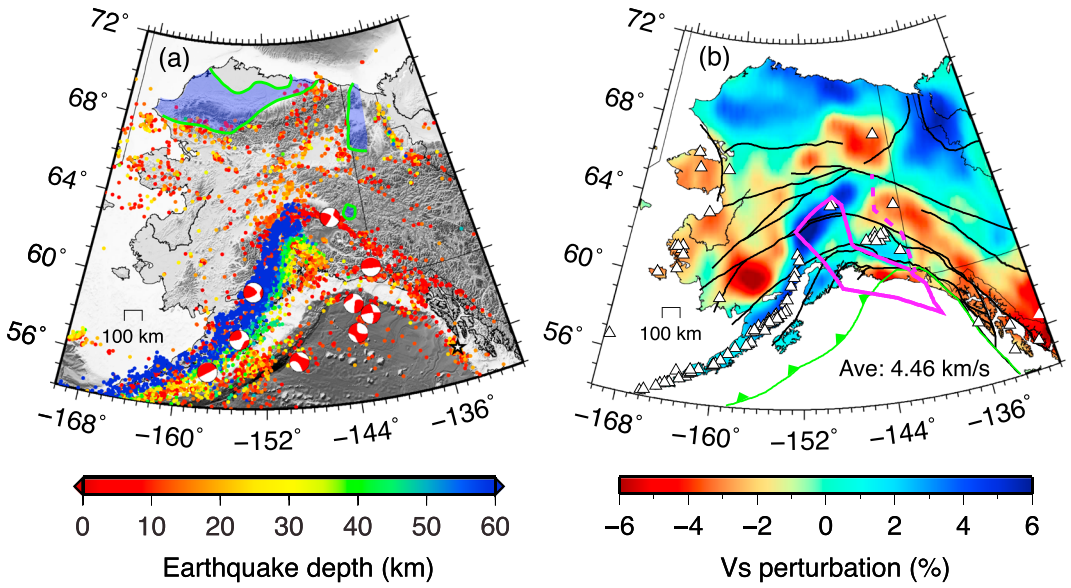

Figure 2. Maps of seismicity and upper mantle Vs (averaged at 55- to 210-km depths). Hypocenters in (a) are from $M > 3.0$ earthquakes between 2000 and 2015 from the Alaska Earthquake Center (AEC) catalog. Moment tensor estimates are from the GCMT catalog (Ekström et al., 2012) for earthquakes of $M_w > 7.0$ since 1976. The blue-shaded regions in (a) represent surface heat flow <60 mW/m^2 from Batir et al., (2016). Volcanoes in (b) are denoted by white triangles. Pink lines indicate the previously resolved extent of the subducted Yakutat terrane, and the dashed segment represents its hypothetical eastern limit from Eberhart-Phillips et al. (2006).

2. Data and Methods

This study benefits from >450 seismic stations deployed across Alaska and northwest Canada between 1999 and 2018 (Figure 1). The stations are from long-term monitoring networks, the TA, and a series of temporary seismic experiments including: Broadband Experiment Across the Alaska Range (BEAAR; Stachnik et al., 2004), Multidisciplinary Observations Of Subduction (MOOS; Kim et al., 2014), Observational and Theoretical Constraints on the Structure and Rotation of the Inner Core (ARCTIC; Lindner et al., 2010), and St. Elias Erosion/Tectonics Project (STEEP; Bauer et al., 2014). Further details on data sources are in the supporting information. Seismic recordings of continuous noise and teleseismic earthquakes are both used in this study.

2.1. Rayleigh Wave Phase Velocities

Rayleigh waves have strong sensitivity to depth-dependent lithospheric structures (e.g., Yang & Forsyth, 2006), complementary to the teleseismic *S* waves that provide sharper lateral resolution but poorer depth resolution (e.g., Schmandt & Humphreys, 2010). In this study, we used 8- to100-s period Rayleigh wave dispersion measurements to constrain the lithospheric Vs structure (Figure S1). The 8- to 30-s-period measurements were taken from the crustal tomography study of Ward and Lin (2018). Longer-period surface waves (30–100 s) were obtained from teleseismic earthquakes. Preprocessing procedures for the teleseismic earthquake data are briefly introduced below.

Broadband waveforms were obtained for all teleseismic events with $M_s > 5.0$ and epicentral distance >1,000 km (Figure S2a) between January 2015 and January 2018. After correction for instrument response, the frequency-time analysis method (Levshin & Ritzwoller, 2001) was used to isolate fundamental mode Rayleigh waves and measure their phase and amplitude information. Phase velocity measurements with signal-to-noise ratio (as defined in Bensen et al., 2007) < 10 were discarded and the remaining measurements were inverted for 2-D phase velocity maps at 30- to 100-s periods on a 0.2° (longitude) × 0.1° (latitude) geographic grid using the Helmholtz tomography method (Lin & Ritzwoller, 2011).

2.2. *S* Wave Travel Time Residuals

The second data source for the Vs inversion is teleseismic *S* wave relative travel time residuals. We obtained broadband waveforms for ~650 teleseismic events with $M_b > 5.5$ and epicentral distance between 28° and

82° for direct *S* and 90–130° for *SKS* phases (Figure S2b). *S* wave data were rotated to radial and transverse components, and relative travel times were measured on the transverse component for direct *S* phases and on the radial component for *SKS* phases. Raw waveforms were visually inspected to ensure clear and coherent waveforms across the array before the multichannel waveform cross-correlation method of VanDecar and Crosson (1990) was used to measure relative residual times for center frequencies of 0.4, 0.1, and 0.05 Hz. A total of >86,000 residual time measurements were obtained for tomography: 53% at 0.05 Hz, 39% at 0.1 Hz, and 8% at 0.4 Hz. The *S* wave measurements were combined with the Rayleigh wave phase velocity maps described in the previous subsection to jointly invert for 3-D Vs structure.

2.3. Joint Rayleigh and *S* Wave Tomography

The Rayleigh and *S* wave tomography approach used here closely follows Jiang et al. (2018), and a 3-D absolute Vs model (0–210 km) is first estimated with a Markov Chain Monte Carlo inversion (Shen et al., 2012) of Rayleigh wave phase velocities. The resulting model (Figure S3) is then used to jointly invert both the Rayleigh and *S* wave data with a conjugate gradient solver, LSQR (Paige & Saunders, 1982). Creating a 3-D starting model for the joint inversion helps to achieve a final 3-D model that maintains high-resolution crustal velocity variations that may be poorly recovered by least squares inversion with a 1-D Vs starting model. The joint inversion method of Jiang et al. (2018) uses approximate finite-frequency travel time sensitivity kernels for *S* waves (Schmandt & Humphreys, 2010) and 1-D phase velocity kernels for Rayleigh waves calculated with the Computer Programs for Seismology package (Herrmann, 2013). The joint inversion solves for isotropic model perturbations relative to the 3-D Vs starting model at 0- to 210-km depth, which was smoothly merged with the AK135 global reference model down to 800 km (Kennett et al., 1995). Structure at depths <50 km was held fixed to the starting model to maintain the high-resolution shallow structure resolved by Ward and Lin (2018). Note that the mix of transverse and radial *S* wave times (*S* and *SKS*, respectively) and Rayleigh waves used in the study have different sensitivities to anisotropy. Eventual comparison with tomography models using Rayleigh and Love waves and inverting for radial and/or azimuthal anisotropy will help to identify areas where strong anisotropy may bias the results of our isotropic inversion. More details on the inversion and optimization procedures can be found in the supporting information.

Two technical improvements were made to the inversion scheme used in this study compared to Jiang et al. (2018). Iterative 3-D ray tracing was implemented with the fast-marching method of de Kool et al. (2006), and azimuthal weighting parameters were introduced to mitigate the bias from the uneven distribution of earthquakes for *S* wave measurements. For the 3-D ray tracing, paths were updated 3 times between LSQR iterations, and tests with additional ray path updates showed stable results similar to prior studies (e.g., Bezada et al., 2013). An example of the deviations from the initial 1-D ray paths is shown in Figure S5. Changes due to 3-D ray tracing are generally subtle, but this more accurate approach accounts for ray paths being pulled toward high-velocity anomalies and away from low-velocity anomalies (Figure S6). To reduce azimuthal bias in the inversion, teleseismic *S* wave measurements from each 60° back-azimuthal bin and their corresponding sensitivity kernels were scaled by weights equal to the number of events in the bin divided by the mean of the number of events in the six bins.

2.4. Synthetic Resolution Tests

Two types of synthetic tests were performed to assess the model resolution, including a checkerboard input and two hypothetical slab inputs. Checkerboard test (Figure S7) demonstrates that the inversion scheme can recover structures with length-scales of ~150 km throughout the upper mantle. The synthetic tests with hypothetical slabs indicate that the model can constrain a subducted slab with a lateral dimension of 120–150 km and distinguish between a continuous slab and a ~120-km-wide slab tear separating the Yakutat shallow-dip slab from the high-velocity anomaly deeper beneath the Wrangell volcanic field (Figures S8 and S9). However, due to the parameterization, our inversion scheme could overestimate the slab thickness if it is narrower than 120 km. Teleseismic and local *P* wave signals can be observed at higher frequencies and thus may be able to sharpen slab resolution in future studies.

3. Results

The final joint inversion yielded a 3-D Vs model achieving variance reduction of 65.1% for *S* wave and 73.8% for Rayleigh wave data. Maps and cross sections of the Vs model presented here show some key features of

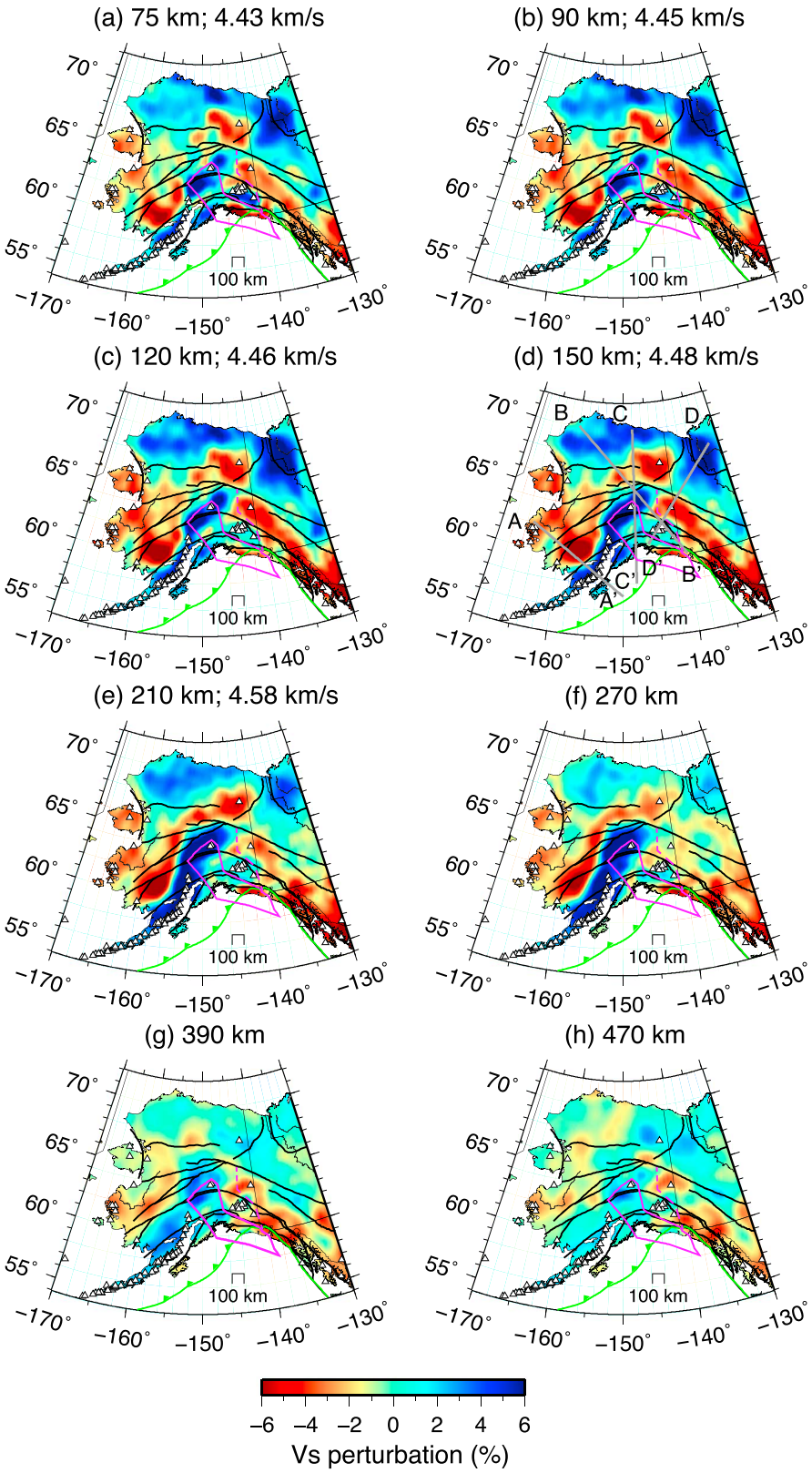

Figure 3. Vs models from the joint inversion plotted at various upper mantle depths. Note that our data are insensitive to absolute Vs below 210-km depths, so regional average Vs is only labeled for (a)–(e). The gray lines in (d) show transect locations in Figure 4.

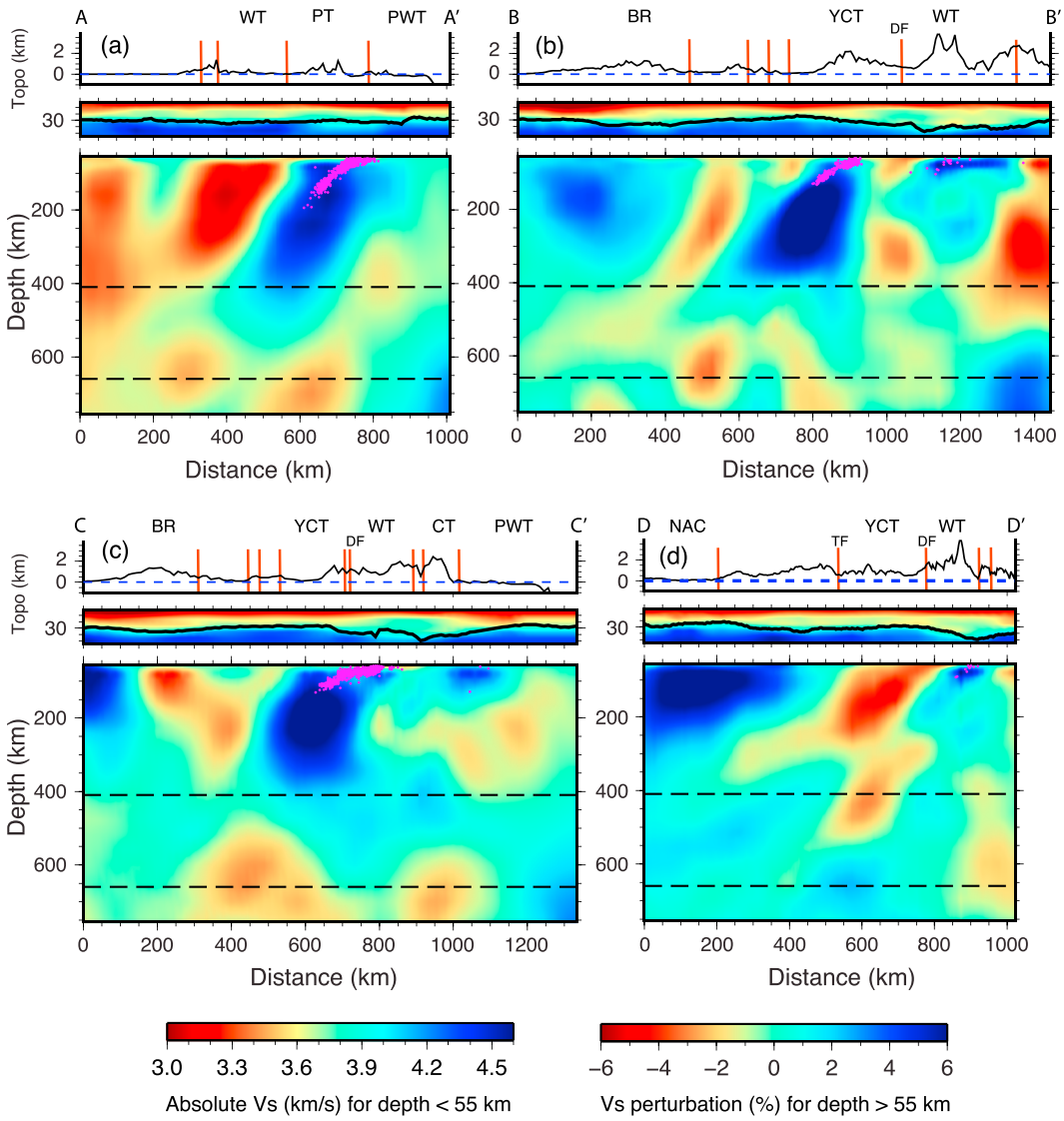

Figure 4. Vertical cross sections of the model at locations marked in Figure 3d (2.5X exaggeration for the vertical axis). Each transect shows the topography variation (top), the absolute vs variation at 0- to 55-km depths (middle), and the Vs perturbation at 55- to 750-km depths (bottom). The thick black lines in the crustal section show the Moho variation (using 4.0 km/s contour from the model of Ward & Lin, 2018). The black dashed lines in the mantle section denote 410- and 660-km depths. The pink circles indicate earthquake hypocenters (Alaska Earthquake Center catalog) located within 10 km. The orange lines denote the main faults shown in Figure 1. More cross sections can be found in the supporting information (Figure S10).

the new model continuously covering mainland Alaska and northwestern Canada (Figures 2b, 3, 4, and S10). Ideally, detailed resolution assessments should be performed at each depth to mask the poorly resolved regions for plotting purpose. For simplicity, we mask out all offshore regions given the relatively uniform onshore coverage of the TA. The full 3-D Vs model, containing the offshore regions, is available for download through the IRIS Earth Model Collaboration (Trabant et al., 2012).

In the shallow upper mantle (<200-km depth) of the plate interior, the new Vs model shows a major structural contrast with lower Vs (~4.2–4.3 km/s) south of the Brooks Range and southwest of the Tintina fault along the transform margin (Figures 3a–3c). Beneath the Brooks Range, in the northern coast of Alaska, and the low-elevation cratonic portion of northwestern Canada, higher Vs (~4.6–4.7 km/s) upper mantle extends to ~210-km depth. Beneath the western Mackenzie Mountains, where the station distribution is sparser and more irregular, intermediate Vs (~4.4–4.6 km/s) is found.

The strongest Vs anomaly at most upper mantle depths is the elongated and northwest-dipping high-velocity region that is spatially correlated with abundant intermediate-depth seismicity attributed to the Pacific plate subduction (Figures 2–4). This anomaly is most prominent at depths of 120–390 km in southern Alaska. The large-scale geometry of the slab is a subject of much prior imaging, and our results are largely consistent with recent studies (Wang & Tape, 2014; Martin-Short et al., 2016), because many southern Alaska TA stations are part of the long-term seismic network in Alaska. Here with augmented data, joint inversion of Rayleigh and *S* waves, and 3-D ray tracing, we find subtle differences such as a particularly sharp bend in the slab at its transition from normal to shallow dip near the longitude of ~ − 152°W (Figures 3a–3c). The high-Vs slab anomalies from the normal and shallow-dip segments of the subduction zone meet with an abrupt kink at ~120- to 150-km depth and an increasingly smooth transition at greater depths (Figure 2). The flat-slab section extends northeastward to ~145°W, farther inboard than previously imaged (e.g., Eberhart-Phillips et al., 2006).

East of the shallow-dip Yakutat slab, our new results show a high-Vs feature beneath the Wrangell volcanic field. The Vs anomaly under the Wrangell volcanic field is generally subtler (~3%) than that of the slab farther west (~6%). At ~200-km depth the shallow-dip slab segment extending north to the Denali fault is clearly offset from the high-Vs anomaly beneath the Wrangell volcanic field. It is possible that they are connected at shallower depths closer to the coast. However, shallower connectivity remains ambiguous due to the limited horizontal resolution (~100 km). The high-Vs feature beneath the Wrangell volcanic field contrasts strongly with the low Vs farther southeast along the transform boundary, indicating a distinctive structure in the upper mantle landward of the Yakutat collision.

4. Discussion

4.1. Continental Upper Mantle Provinces

The upper mantle Vs model in this study newly covers the entire Alaskan mainland and part of northwestern Canada allowing a more comprehensive exploration of lithospheric structure. One of the clearest new results is that the western Brooks Range and Arctic coast are underlain by a high Vs (~4.6–4.7 km/s) mantle root (Figures 2b and 3a–3e). This indication of cold and thick lithosphere is consistent with recent seismic imaging of deep lithospheric discontinuities using Sp receiver functions (O'Driscoll & Miller, 2015) and low surface heat flow ($<$60 mW/m^2 in Figure 2a; Batir et al., 2016). Additionally, prior interpretation of a magnetic boundary at the southern edge of the Brooks Range favored the presence of a voluminous mafic layer in the crust which may be complemented by a melt-depleted mantle root (Saltus & Hudson, 2007). The cold thick lithosphere of northern Alaska imaged here likely acts as a strong block that guides tectonic deformation farther south across the Alaskan mainland (O'Driscoll & Miller, 2015; Redfield et al., 2007; Saltus & Hudson, 2007), where our Vs model shows slow Vs (~4.25–4.4 km/s) in the upper mantle. Distributed Quaternary volcanic fields along the western coast of Alaska are generally underlain by slower than average mantle Vs (Miller et al., 1998), consistent with near-solidus temperatures. The lower-Vs upper mantle of southern Alaska locally extends to near the Arctic coast along the Alaska-Yukon Territory boundary, where it coincides with isolated Quaternary magmatism and separates thick high-Vs lithosphere beneath northern Alaska and the northern Yukon (Figure 2b).

4.2. Geometry of Ongoing Subduction

The high-Vs Pacific slab dips steeply beneath the Aleutian arc extending east until near the longitude of ~ − 152°W, where the high-Vs anomaly exhibits a dramatic kink. The kink in the slab appears sharpest at ~120–150 km (Figures 3b and 3c) and becomes more gradual at greater depths (Figures 3d–3f). Such an along-strike transition is also seen in the pattern of seismicity (Figure 2a) and it is coincident with prior interpretations of the western edge of shallow-dip subduction of the Yakutat terrane (Eberhart-Phillips et al., 2006). The sharp change of slab dip could be associated with development of a slab tear, although the two slab segments appear continuous at depths $>$ ~175 km, consistent with the prior teleseismic body wave tomography (Martin-Short et al., 2016). Additionally, teleseismic scattered wave imaging (Kim et al., 2014) and an active source profile (Fuis et al., 2008) indicate that the two slab segments overlap with each other at the contact region.

Similar to prior studies we find that most of the shallow-dip slab segment transitions to a steeper dip angle near the Denali fault (Figure 4; Martin-Short et al., 2016; Wang & Tape, 2014). Closer to the subduction zone at ~50–100 km depth we find high Vs indicative of cold upper mantle in the inferred location of the shallow-dip Yakutat slab (Eberhart-Phillips et al., 2006). The high Vs (~4.55 km/s) uppermost mantle that we find is consistent with the interpretation that the Denali volcanic gap exists due to inboard advance of a cold slab that prevents melt generation (Rondenay et al., 2010). At its northeastern edge the shallow-dip slab section extends ~100 km farther inboard than previously imaged but is still within the limits of the potential Yakutat slab predicted by Eberhart-Phillips et al. (2006) using reconstructed plate motions. This positioning suggests a slightly earlier onset of shallow-dip subduction by ~20 Ma (Eberhart-Phillips et al., 2006), which is consistent with geologic evidence that Yakutat flat subduction likely initiated by ~26 Ma (Benowitz et al., 2011; Finzel et al., 2015).

4.3. Potential Slab Fragment Beneath the Wrangell Volcanic Field

The high-Vs feature beneath the Wrangell volcanic field sits landward of the eastern portion of the Yakutat terrane where subduction has likely slowed as a result of eastward thickening of the Yakutat terrane's buoyant crust (Worthington et al., 2012) leading to accommodation of Pacific-North America convergence by upper plate shortening (e.g., Elliot et al., 2013). Prior investigation of earthquake hypocenters indicates a Wrangell slab that transitions from a shallow to steep dip angle at ~70-km depth (Page et al., 1989). We suggest that the high-Vs anomaly beneath the Wrangell volcanic field represents a slab segment that subducted on the leading edge of the Yakutat terrane and is sinking near-vertically beneath the volcanic field, because subduction has slowed down due to the Yakutat collision.

The presence of the high-Vs anomaly beneath the Wrangell volcanic field is robust based on synthetic tests, but the nature of its connection to ongoing subduction to the west is less clear and likely varies with depth. At ~200-km depth, it is well separated from the ongoing shallow-dip slab to the west indicating an evolving slab tear (Figure 3). At shallower depths ($<$150 km) and closer to the coast the hypothesized Wrangell slab segment may still be connected to the active shallow-dip slab that extends beneath the Alaska Range. A recent study of tectonic tremor suggests an eastward continuation of subduction (Wech, 2016) beyond the boundary of the earthquake hypocenters used to define the Slab 1.0 model (Hayes et al., 2012; Figure 1). Our results suggest that such a slab fragment extends farther east, but only a small fraction of it may be in contact with the base of the upper plate as it sinks due to eastward slowing of Yakutat subduction (e.g., Bruhn et al., 2004; Elliot et al., 2013).

The subtler Vs anomaly of the inferred Wrangell slab may have multiple contributions including the eastward decrease in age of the incoming Pacific seafloor (Müller et al., 2008), slowing of subduction leading to a warmer slab at a given depth compared to the slab farther west, and tearing that allows inflow of asthenosphere weakening the Vs anomaly when averaged over $>$100-km length scales. Petrology and geochemistry investigations of Wrangell magmatism are consistent with heterogeneous contributions from slab-derived fluids (Preece & Hart, 2004; Skulski et al., 1991), but it is possible that mantle flow could deliver some subduction influence even in the absence of a Wrangell slab segment (Jadamec et al., 2013). Based on the new tomography, we suggest there is merit in further scrutinizing the geometry of the potential Wrangell slab fragment and its connectivity to the shallow-dip Yakutat slab to the west. It may present an opportunity for detailed investigation of an actively evolving slab tear.

5. Conclusions

We have constructed a new upper mantle Vs model of Alaska and northwestern Canada using teleseismic *S* waves and Rayleigh waves. The model highlights distinct lithospheric provinces in the plate interior including two provinces of thick high-Vs lithosphere in northern Alaska and the Yukon Territory, where cold strong blocks could limit large-scale transpressional deformation to regions farther south that have thinner and warmer lithosphere. The shallow-dip Yakutat slab extends further northeastward than previously imaged and marks abrupt transitions in subduction zone structure. To the west, a kink in the slab is imaged at $<$150-km depth, but the deeper slab appears continuous. To the east, a subtler high-Vs anomaly is imaged beneath the Wrangell volcanic field. It appears separated from the shallow-dip slab suggesting slab contributions to Wrangell magmatism and the possibility of a growing slab tear due to the ongoing Yakutat collision with the St. Elias Mountains.

Acknowledgments
All seismic data used in the study are publicly available from the IRIS DMC (https://ds.iris.edu/ds/nodes/dmc/). The 3-D Vs model produced in the study, named Alaska-Joint-S-SW is available via the IRIS EMC (http://ds.iris.edu/ds/products/emc/) at the time of publication. This research was supported by NSF EAR 1554908 (B. S.) and EAR 1753362 (F. C. L.). We thank Carl Tape, an anonymous reviewer, and the Editor for their helpful feedback.

References

Batir, J. F., Blackwell, D. D., & Richards, M. C. (2016). Heat flow and temperature-depth curves throughout Alaska: Finding regions for future geothermal exploration. *Journal of Geophysics and Engineering*, *13*(3), 366–378. https://doi.org/10.1088/1742-2132/13/3/366

Bauer, M. A., Pavlis, G. L., & Landes, M. (2014). Subduction geometry of the Yakutat terrane, southeastern Alaska. *Geosphere*, *10*(6), 1161–1176. https://doi.org/10.1130/GES00852.1

Benowitz, J. A., Layer, P. W., Armstrong, P., Perry, S. E., Haeussler, P. J., Fitzgerald, P. G., & et al. (2011). Spatial variations in focused exhumation along a continental-scale strike-slip fault: The Denali fault of the eastern Alaska Range. *Geosphere*, *7*(2), 455–467. https://doi.org/10.1130/GES00589.1

Bensen, G. D., Ritzwoller, M. H., Barmin, M. P., Levshin, A. L., Lin, F., Moschetti, M. P., et al. (2007). Processing seismic ambient noise data to obtain reliable broad-band surface wave dispersion measurements. *Geophysical Journal International*, *169*(3), 1239–1260. https://doi.org/10.1111/j.1365-246X.2007.03374.x

Bezada, M. J., Humphreys, E. D., Toomey, D. R., Harnafi, M., Dávila, J. M., & Gallart, J. (2013). Evidence for slab rollback in westernmost Mediterranean from improved upper mantle imaging. *Earth and Planetary Science Letters*, *368*, 51–60. https://doi.org/10.1016/j.epsl.2013.02.024

Bruhn, R. L., Pavlis, T. L., Plafker, G., & Serpa, L. (2004). Deformation during terrane accretion in the Saint Elias orogen, Alaska. *Geological Society of America Bulletin*, *116*(7), 771–787. https://doi.org/10.1130/B25182.1

Coulson, S., Garth, T., & Rietbrock, A. (2018). Velocity structure of the subducted Yakutat terrane, Alaska: Insights from guided waves. *Geophysical Research Letters*, *45*, 3420–3428. https:// doi.org/10.1002/2017GL076583

de Kool, M., Rawlinson, N., & Sambridge, M. (2006). A practical grid-based method for tracking multiple refraction and reflection phases in three-dimensional heterogeneous media. *Geophysical Journal International*, *167*(1), 253–270. https://doi.org/10.1111/j.1365-246X.2006.03078.x

DeMets, C., & Dixon, T. H. (1999). New kinematic models for Pacific-North America motion from 3 Ma to present, I: Evidence for steady motion and biases in the NUVEL-1A model. *Geophysical Research Letters*, *26*(13), 1921–1924. https://doi.org/10.1029/1999GL900405

Eberhart-Phillips, D., Christensen, D. H., Brocher, T. M., Hansen, R., Ruppert, N. A., Haeussler, P. J., & et al. (2006). Imaging the transition from Aleutian subduction to Yakutat collision in Central Alaska, with local earthquakes and active source data. *Journal of Geophysical Research*, *111*, B11303. https://doi.org/10.1029/2005JB004240

Ekström, G., Nettles, M., & Dziewoński, A. M. (2012). The global CMT project 2004–2010: Centroid-moment tensors for 13,017 earthquakes. *Physics of the Earth and Planetary Interiors*, *200*, 1–9.

Elliott, J., Freymueller, J. T., & Larsen, C. F. (2013). Active tectonics of the St. Elias orogen, Alaska, observed with GPS measurements. *Journal of Geophysical Research: Solid Earth*, *118*, 5625–5642. https://doi.org/10.1002/jgrb.50341

Elliott, J. L., Larsen, C. F., Freymueller, J. T., & Motyka, R. J. (2010). Tectonic block motion and glacial isostatic adjustment in Southeast Alaska and adjacent Canada constrained by GPS measurements. *Journal of Geophysical Research*, *115*, B09407. https://doi.org/10.1029/2009JB007139

Enkelmann, E., Koons, P. O., Pavlis, T. L., Hallet, B., Barker, A., Elliott, J., et al. (2015). Cooperation among tectonic and surface processes in the St. Elias Range, Earth's highest coastal mountains. *Geophysical Research Letters*, *42*, 5838–5846. https://doi.org/10.1002/2015GL064727

Finzel, E. S., Ridgway, K. D., & Trop, J. M. (2015). Provenance signature of changing plate boundary conditions along a convergent margin: Detrital record of spreading-ridge and flat-slab subduction processes, Cenozoic forearc basins, Alaska. *Geosphere*, *11*(3), 823–849. https://doi.org/10.1130/GES01029.1

Fuis, G. S., Moore, T. E., Plafker, G., Brocher, T. M., Fisher, M. A., Mooney, W. D., et al. (2008). Trans-Alaska Crustal Transect and continental evolution involving subduction underplating and synchronous foreland thrusting. *Geology*, *36*(3), 267–270. https://doi.org/10.1130/G24257A.1

Golos, E. M., Fang, H., Yao, H., Zhang, H., Burdick, S., Vernon, F., et al. (2018). Shear-wave tomography beneath the United States using a joint inversion of surface and body waves. *Journal of Geophysical Research: Solid Earth*, *123*, 5169–5189. https://doi.org/10.1029/2017JB014894

Guo, Z., Wang, K., Yang, Y., Tang, Y., John Chen, Y., & Hung, S. H. (2018). The origin and mantle dynamics of quaternary intraplate volcanism in Northeast China from joint inversion of surface wave and body wave. *Journal of Geophysical Research: Solid Earth*, *123*, 2410–2425. https://doi.org/10.1002/2017JB014948

Haeussler, P. J. (2008). An overview of the neotectonics of interior Alaska: Far-field deformation from the Yakutat microplate collision. In J. T. Freymueller, et al. (Eds.), *Active tectonics and seismic potential of Alaska*, *Geophys. Monogr. Ser.*, (Vol. 179, pp. 83–108). Washington, D. C: American Geophysical Union.

Hayes, G. P., Wald, D. J., & Johnson, R. L. (2012). Slab1. 0: A three-dimensional model of global subduction zone geometries. *Journal of Geophysical Research*, *117*, B01302. https://doi.org/10.1029/2011JB008524

Herrmann, R. B. (2013). Computer programs in seismology: An evolving tool for instruction and research. *Seismological Research Letters*, *84*(6), 1081–1088. https://doi.org/10.1785/0220110096

Jadamec, M. A., Billen, M. I., & Roeske, S. M. (2013). Three-dimensional numerical models of flat slab subduction and the Denali fault driving deformation in south-Central Alaska. *Earth and Planetary Science Letters*, *376*, 29–42. https://doi.org/10.1016/j.epsl.2013.06.009

Jiang, C., Schmandt, B., Hansen, S. M., Dougherty, S. L., Clayton, R. W., Farrell, J., & et al. (2018). Rayleigh and *S* wave tomography constraints on subduction termination and lithospheric foundering in Central California. *Earth and Planetary Science Letters*, *488*, 14–26. https://doi.org/10.1016/j.epsl.2018.02.009

Kennett, B. L. N., Engdahl, E. R., & Buland, R. (1995). Constraints on seismic velocities in the Earth from traveltimes. *Geophysical Journal International*, *122*(1), 108–124. https://doi.org/10.1111/j.1365-246X.1995.tb03540.x

Kim, Y., Abers, G. A., Li, J., Christensen, D., Calkins, J., & Rondenay, S. (2014). Alaska megathrust 2: Imaging the megathrust zone and Yakutat/Pacific plate interface in the Alaska subduction zone. *Journal of Geophysical Research: Solid Earth*, *119*, 1924–1941. https://doi.org/10.1002/2013JB010581

Leonard, L. J., Mazzotti, S., & Hyndman, R. D. (2008). Deformation rates estimated from earthquakes in the northern cordillera of Canada and eastern Alaska. *Journal of Geophysical Research*, *113*, B08406. https://doi.org/10.1029/2007JB005456

Levshin, A. L., & Ritzwoller, M. H. (2001). Automated detection, extraction, and measurement of regional surface waves. In *Monitoring the comprehensive nuclear-test-ban treaty: Surface waves*, (pp. 1531–1545). Basel: Birkhäuser. https://doi.org/10.1007/978-3-0348-8264-4_11

Lin, F. C., & Ritzwoller, M. H. (2011). Helmholtz surface wave tomography for isotropic and azimuthally anisotropic structure. *Geophysical Journal International*, *186*(3), 1104–1120. https://doi.org/10.1111/j.1365-246x.2011.05070.x

Lindner, D., Song, X., Ma, P., & Christensen, D. H. (2010). Inner core rotation and its variability from nonparametric modeling. *Journal of Geophysical Research*, *115*, B04307. https://doi.org/10.1029/2009jb006294

Marechal, A., Mazzotti, S., Elliott, J. L., Freymueller, J. T., & Schmidt, M. (2015). Indentor-corner tectonics in the Yakutat-St. Elias collision constrained by GPS. *Journal of Geophysical Research: Solid Earth*, *120*, 3897–3908. https://doi.org/10.1002/2014JB011842

Martin-Short, R., Allen, R. M., & Bastow, I. D. (2016). Subduction geometry beneath south central Alaska and its relationship to volcanism. *Geophysical Research Letters*, *43*, 9509–9517. https://doi.org/10.1002/2016GL070580

Mazzotti, S., & Hyndman, R. D. (2002). Yakutat collision and strain transfer across the northern Canadian cordillera. *Geology*, *30*(6), 495–498. https://doi.org/10.1130/0091-7613(2002)030<0495:YCASTA>2.0.CO;2

McNamara, D. E., & Pasyanos, M. E. (2002). Seismological evidence for a sub-volcanic arc mantle wedge beneath the Denali volcanic gap, Alaska. *Geophysical Research Letters*, *29*(16), 1814. https://doi.org/10.1029/2001GL014088

Miller, T. P., McGimsey, R. G., Richter, D. H., Riehle, J. R., Nye, C. J., Yount, M. E., & et al. (1998). Catalog of the historically active volcanoes of Alaska. US Geological Survey Open-File Report, 98, 104.

Müller, R. D., Sdrolias, M., Gaina, C., & Roest, W. R. (2008). Age, spreading rates, and spreading asymmetry of the world's ocean crust. *Geochemistry, Geophysics, Geosystems*, *9*, Q04006. https://doi.org/10.1029/2007GC001743

Obrebski, M., Allen, R. M., Pollitz, F., & Hung, S. H. (2011). Lithosphere–asthenosphere interaction beneath the western United States from the joint inversion of body-wave traveltimes and surface-wave phase velocities. *Geophysical Journal International*, *185*(2), 1003–1021. https://doi.org/10.1111/j.1365-246X.2011.04990.x

O'Driscoll, L. J., & Miller, M. S. (2015). Lithospheric discontinuity structure in Alaska, thickness variations determined by Sp receiver functions. *Tectonics*, *34*, 694–714. https://doi.org/10.1002/2014tc003669

Page, R. A., Stephens, C. D., & Lahr, J. C. (1989). Seismicity of the Wrangell and Aleutian Wadati-Benioff zones and the north American plate along the trans-Alaska crustal transect, Chugach Mountains and Copper River basin, southern Alaska. *Journal of Geophysical Research*, *94*(B11), 16059–16082. https://doi.org/10.1029/JB094iB11p16059

Paige, C. C., & Saunders, M. A. (1982). LSQR: An algorithm for sparse linear equations and sparse least squares. *ACM Transactions on Mathematical Software*, *8*(1), 43–71. https://doi.org/10.1145/355984.355989

Plafker, G., & Berg, H. C. (1994). Overview of the geology and tectonic evolution of Alaska. In G. Plafker, & H. C. Berg (Eds.), *The geology of North America*, *The Geology of Alaska*, Chap 33, (Vol. G-1, pp. 989–1021).

Preece, S. J., & Hart, W. K. (2004). Geochemical variations in the< 5 Ma Wrangell volcanic field, Alaska: Implications for the magmatic and tectonic development of a complex continental arc system. *Tectonophysics*, *392*(1–4), 165–191. https://doi.org/10.1016/j.tecto.2004.04.011

Redfield, T. F., Scholl, D. W., Fitzgerald, P. G., & Beck, M. E., Jr. (2007). Escape tectonics and the extrusion of Alaska: Past, present, and future. *Geology*, *35*(11), 1039–1042. https://doi.org/10.1130/g23799a.1

Richter, D. H., Smith, J. G., Lanphere, M. A., Dalrymple, G. B., Reed, B. L., & Shew, N. (1990). Age and progression of volcanism, Wrangell volcanic field, Alaska. *Bulletin of Volcanology*, *53*(1), 29–44. https://doi.org/10.1007/BF00680318

Rondenay, S., Montési, L. G., & Abers, G. A. (2010). New geophysical insight into the origin of the Denali volcanic gap. *Geophysical Journal International*, *182*(2), 613–630. https://doi.org/10.1111/j.1365-246x.2010.04659.x

Saltus, R. W., & Hudson, T. L. (2007). Regional magnetic anomalies, crustal strength, and the location of the northern Cordilleran fold-and-thrust belt. *Geology*, *35*(6), 567–570. https://doi.org/10.1130/G23470A.1

Schmandt, B., & Humphreys, E. (2010). Seismic heterogeneity and small-scale convection in the southern California upper mantle. *Geochemistry, Geophysics, Geosystems*, *11*, Q05004. https://doi.org/10.1029/2010GC003042

Shen, W., Ritzwoller, M. H., Schulte-Pelkum, V., & Lin, F. C. (2012). Joint inversion of surface wave dispersion and receiver functions: A Bayesian Monte-Carlo approach. *Geophysical Journal International*, *192*(2), 807–836. https://doi.org/10.1093/gji/ggs050

Skulski, T., Francis, D., & Ludden, J. (1991). Arc-transform magmatism in the Wrangell volcanic belt. *Geology*, *19*(1), 11–14. https://doi.org/10.1130/0091-7613(1991)019<0011:ATMITW>2.3.CO;2

Spotila, J. A., & Berger, A. L. (2010). Exhumation at orogenic indentor corners under long-term glacial conditions: Example of the St. Elias orogen, southern Alaska. *Tectonophysics*, *490*(3–4), 241–256. https://doi.org/10.1016/j.tecto.2010.05.015

Stachnik, J. C., Abers, G. A., & Christensen, D. H. (2004). Seismic attenuation and mantle wedge temperatures in the Alaska subduction zone. *Journal of Geophysical Research*, *109*, B10304. https://doi.org/10.1029/2004JB003018

Trabant, C., Hutko, A. R., Bahavar, M., Karstens, R., Ahern, T., & Aster, R. (2012). Data products at the IRIS DMC: Stepping stones for research and other applications. *Seismological Research Letters*, *83*(5), 846–854. https://doi.org/10.1785/0220120032

Trop, J. M., & Ridgway, K. D. (2007). Mesozoic and Cenozoic tectonic growth of southern Alaska: A sedimentary basin perspective. In K. D. Ridgway, J. M. Trop, J. M. G. Glen, & J. M. O'Neil (Eds.), *Tectonic growth of a collisional continental margin—Crustal evolution of Southern Alaska*, *Special papers*, (Vol. 431, pp. 55–94). America: Geological society.

VanDecar, J. C., & Crosson, R. S. (1990). Determination of teleseismic relative phase arrival times using multi-channel cross-correlation and least squares. *Bulletin of the Seismological Society of America*, *80*(1), 150–169.

Wang, Y., & Tape, C. (2014). Seismic velocity structure and anisotropy of the Alaska subduction zone based on surface wave tomography. *Journal of Geophysical Research: Solid Earth*, *119*, 8845–8865. https://doi.org/10.1002/2014JB011438

Ward, K. M., & Lin, F. (2018). Lithospheric structure across the Alaskan cordillera from the joint inversion of surface waves and receiver functions. *Journal of Geophysical Research: Solid Earth*, *123*. https://doi.org/10.1029/2018JB015967

Wech, A. G. (2016). Extending Alaska's plate boundary: Tectonic tremor generated by Yakutat subduction. *Geology*, *44*(7), 587–590. https://doi.org/10.1130/g37817.1

West, M., Gao, W., & Grand, S. (2004). A simple approach to the joint inversion of seismic body and surface waves applied to the southwest US. *Geophysical Research Letters*, *31*, L15615. https://doi.org/10.1029/2004GL020373

Worthington, L. L., Van Avendonk, H. J., Gulick, S. P., Christeson, G. L., & Pavlis, T. L. (2012). Crustal structure of the Yakutat terrane and the evolution of subduction and collision in southern Alaska. *Journal of Geophysical Research*, *117*, B01102. https://doi.org/10.1029/2011JB008493

Yang, Y., & Forsyth, D. W. (2006). Regional tomographic inversion of the amplitude and phase of Rayleigh waves with 2-D sensitivity kernels. *Geophysical Journal International*, *166*(3), 1148–1160. https://doi.org/10.1111/j.1365-246X.2006.02972.x

You, T., & Zhao, D. (2012). Seismic anisotropy and heterogeneity in the Alaska subduction zone. *Geophysical Journal International*, *190*(1), 629–649. https://doi.org/10.1111/j.1365-246x.2012.05512.x

Zhao, D., Christensen, D., & Pulpan, H. (1995). Tomographic imaging of the Alaska subduction zone. *Journal of Geophysical Research*, *100*(B4), 6487–6504. https://doi.org/10.1029/95JB00046